RSC Advances

PAPER

View Article Online
View Journal | View Issue

Cite this: *RSC Adv.*, 2020, **10**, 7708

The mineralization, drug release and *in vivo* bone defect repair properties of calcium phosphates/PLA modified tantalum scaffolds†

Rong Zhou,‡[ab] Hai-Jian Ni,‡[c] Jin-Hui Peng,*[a] Ning Liu,[a] Shu Chen,[a] Jia-Hua Shao,[a] Qi-Wei Fu,[a] Jun-Jian Liu,[c] Feng Chen *[c] and Qi-Rong Qian*[a]

Calcium phosphate based biomaterials have been widely studied in biomedical areas. Herein, amorphous calcium phosphate (**ACP**) nanospheres and hydroxyapatite (**HA**) nanorods were separately prepared and used for coating tantalum (**Ta**) scaffolds with a polymer of polylactide (**PLA**). We have found that different crystal phases of calcium phosphate coated on **Ta** scaffolds displayed different effects on the surface morphologies, mineralization and bovine serum albumin (**BSA**) release. The **ACP-PLA** and **HA-PLA** coated on **Ta** scaffold were more favorable for *in vitro* mineralization than bare and **PLA** coated **Ta** scaffolds, and resulted in a highly hydrophilic surfaces. Meanwhile, the osteoblast-like cells (MG63) showed favorable properties of adhesion and spreading on both **ACP-PLA** and **HA-PLA** coated **Ta** scaffolds. The **ACP-PLA** and **HA-PLA** coated **Ta** scaffolds showed a high biocompatibility and potential applications for *in vivo* bone defect repair.

Received 11th November 2019
Accepted 15th February 2020

DOI: 10.1039/c9ra09385k

rsc.li/rsc-advances

1. Introduction

Bone defects originated by trauma and other pathological changes are common clinical diseases. Many strategies have been developed for the therapy of bone defects, including implantation of autografts/allografts and synthetic scaffolds.[1,2] The use of synthetic scaffolds is one of the most promising ways for the treatment of bone defects.[3,4] The synthetic scaffolds have convenient sources, good safety and non-immunogenicity, therefore, various synthetic scaffolds such as inorganic ceramics, bone cements, and metal implants have been introduced as the substrates for bone defects.[5,6] These synthetic scaffolds provide physical support, structural guidance, and sites for cells adhesion, which are very important in new bone tissue regeneration, for example, in the porous tantalum (**Ta**) scaffolds which have been introduced as a metallic implant for bone defect therapy. Porous **Ta** scaffolds haves good stability, high volumetric porosity (70–80%), low modulus of elasticity (3 MPa), and high friction characteristics, which can improve bone ingrowth and bone mineral density.[7–9]

The preparation of ideal biomedical scaffold, which can provide suitable functions such as mechanical support, biocompatibility, osteoconductivity and osteoinductivity, is still a big challenge. Synthesizing a biomaterial with a single component meeting the high requirements of bone defect repair is still difficult. Therefore, composite materials and surface modification have been studied. For example, calcium phosphate (**CaP**) hybrid materials have been developed to improve the mechanical properties, biocompatibility and bioactivity of synthetic scaffolds.[10,11] The **CaP** based materials are considered as promising biomaterials with high biocompatibility and bioactivity, attributed to the similar chemical properties to the mineral phase of bone.[12–14] In native bone tissues, the nanostructured hydroxyapatite (**HA**) can form a hierarchical composite with collagen fibrils.[15,16] Therefore, the synthetic nanostructured **CaP** has been deemed to be biocompatible and hold a good biodegradation.[17,18] **CaP** based biomaterials and their composites have been extensively employed in various biomedical areas, such as drug delivery,[19–21] protein adsorption,[22] bioimaging,[23,24] bone defect repair/tissue engineering.[25,26] For example, **CaP** coated metallic scaffolds are considered as the promising weight bearing implants owing to their advantages of high biocompatibility and strength.[27–29] Meanwhile, in previous studies, the protein drugs of growth factors, such as, morphogenetic protein (**BMP**), vascular endothelial growth factor (**VEGF**), basic fibroblast growth factor (**bFGF**) and transforming growth factor-beta (**TGF-β**), were adopted and loaded in **CaP** materials to prepare biomaterials

[a]*Department of Orthopedics, Changzheng Hospital, Second Military Medical University, Shanghai, 200003, P. R. China. E-mail: pengjinhui20110@smmu.edu.cn; qianqr@smmu.edu.cn*

[b]*Department of Orthopaedics, 72nd Group Army Hospital of PLA, No. 9 Chezhan Road, Wuxing District, Huzhou, 313000, P. R. China*

[c]*Department of Orthopedics, Spinal Pain Research Institute, Shanghai Tenth People's Hospital, Tongji University School of Medicine, Shanghai 200072, P. R. China. E-mail: fchen@tongji.edu.cn*

† Electronic supplementary information (ESI) available. See DOI: 10.1039/c9ra09385k

‡ These authors contributed equally to this work.

which are favorable for bone defect repair.[10,11,30] However, the drug release properties of modified **Ta** scaffolds are rarely reported and still necessary in the biomedical field, especially for the application of bone defect repair.

In this study, the amorphous calcium phosphate (**ACP**) nanospheres and **HA** nanorods have been prepared and separately blended with racemic polylactic acid (**PLA**) to modify **Ta** scaffolds. The physico-chemical properties, mineralization, drug release, cell viability and the effects on bone defect repair of the **ACP-PLA** and **HA-PLA** modified **Ta** scaffolds have been investigated.

2. Experimental

2.1 Preparation of ACP nanospheres and HA nanorods

The **ACP** nanospheres were prepared by a modified method from reported literature.[31] Firstly, the Solution A for reaction was prepared by dissolving $CaCl_2$ (0.166 g) and polylactide-*block*-monomethoxy(polyethyleneglycol) (**PLA-mPEG**) (0.025 g) in deionized water (60 mL). Then, aqueous ammonia (~25%, 10 mL) was added into Solution A. Meanwhile, the Solution B was prepared by dissolving $Na_2HPO_4 \cdot 12H_2O$ (0.355 g) and **PLA-mPEG** (0.025 g) in deionized water (60 mL). Secondly, the Solution A with aqueous ammonia was slowly added (20 mL min^{-1}) into Solution B. The resulting mixed solution was stirred for 1 h at room temperature. Finally, the **ACP** nanospheres were separated by centrifugation, washed with deionized water and ethanol several times. For the preparation of **HA** nanorods, the above reaction solution (60 mL) without separation was transferred to a Teflon-lined stainless steel autoclave (100 mL), sealed, and heated at 200 °C for 24 h. After cooling down to room temperature, the products were separated by centrifugation, and washed with deionized water and ethanol several times. The block copolymer of **PLA-mPEG** ($M_{w\ PLA}$ = 3000, $M_{w\ PEG}$ = 5000) were purchased from Jinan Daigang Biomaterials Co. Ltd. Other chemicals were purchased from Sinopharm Chemical Reagent Co. and used as received without further purification.

2.2 Preparation of ACP-PLA and HA-PLA modified Ta scaffolds

ACP nanospheres and **HA** nanorods were separately dispersed in acetone, and then the equal amount of solid **PLA** polymer were added in the above suspensions under magnetic stirring. After dissolution of **PLA**, the **ACP-PLA** and **HA-PLA** suspensions were obtained for coating **Ta** scaffolds. The concentration of **ACP**, **HA** and **PLA** was separately fixed at 3 wt% in each suspension. The racemic **PLA** (M_w = 500 000) were purchased from Jinan Daigang Biomaterials Co. Ltd. The **Ta** plates (1 cm × 1 cm × 0.1 mm) were obtained from Beijing Orient Tantalum Niobium Co. Ltd. (China). **Ta** scaffolds (0.5 cm × 0.5 cm × 0.5 cm) were obtained from Zimmer Inc. (USA), with a definite porosity of 75–80% and an average pore size of 440 μm. The coating process of **Ta** scaffolds was performed as follows: the clean **Ta** plates and porous **Ta** scaffolds were respectively put into the above **ACP-PLA** and **HA-PLA** suspensions, and kept under shaking at 37 °C for 24 h. Thereafter, the **ACP-PLA** and **HA-PLA** modified **Ta** plates and porous **Ta** scaffolds were obtained through natural drying on filter papers.

Meanwhile, the adsorption efficiency of growth factor by **ACP** nanospheres and **HA** nanorods were studied, and the fluorescein isothiocyanate (**FITC**)-labeled **VEGF** (**VEGF-FITC**) was used. The conjugation process was performed with a FITC Protein Labeling Kit (ThermoFisher Scientific), following the manufacturer's instructions. Briefly, **VEGF** and **FITC** were mixed at a 1 : 60 molar ratio, incubated at room temperature for 2 h in the dark, and dialyzed at 4 °C against **PBS** for 24 h. The **VEGF-FITC** loading experiments were performed as follows: the as-prepared **ACP** nanospheres (30 mg) and **HA** nanorods (30 mg) were separately dispersed in aqueous solution (5 mL) with **VEGF-FITC** (5 μg). The suspension was shaken at a constant rate of 130 rpm in a sealed vessel at 37 °C for 2 h. After centrifugal separation, the supernatants were obtained, and the fluorescence emission spectra of the supernatants were measured in the range from 510 nm to 650 nm with 495 nm of excitation wavelength (F-7000 fluorescence spectrometer, Hitachi Ltd., Japan). The fluorescence micrographs of **VEGF-FITC**-loading **ACP** nanospheres and **HA** nanorods were also obtained by a confocal laser scanning microscopy (Leica, SP8, Germany) to confirm the adsorption of **VEGF-FITC**.

2.3 Characterization of samples

Transmission electron microscopy (TEM) micrographs were taken with a JEOL JEM 2100 field-emission transmission electron microscope. The surface morphology has been observed with a JEOL JSM-6700 field-emission scanning electron microscopy (SEM). X-ray powder diffraction (XRD) patterns were recorded using a Rigaku D/max 2550V X-ray diffractometer with a graphite monochromator (Cu K_α radiation, λ = 1.54178 Å). Fourier transform infrared (FTIR) spectra were taken on a FTIR spectrometer (FTIR-7600, Lambda Scientific, Australia). The thermogravimetric (TG) and differential scanning calorimeter (DSC) analysis was carried out with a STA-409/PC simultaneous thermal analyzer (Netzsch, Germany) at a heating rate of 10 °C min^{-1} in flowing air. The hydrophilic properties were characterized by measuring the contact angles of the **ACP-PLA**, **HA-PLA** modified **Ta** plates before and after the mineralization. The contact angles and the images have been obtained by dropping deionized water (4 μL) on the surface of different samples for 10 seconds, using an Automatic Contact Angle Meter Model SL200A/B/D Series.

2.4 *In vitro* mineralization of ACP-PLA and HA-PLA coatings

The standard simulated body fluid (**SBF**) with a pH of 7.4 has been prepared according to the reported method.[32] **SBF** solution has definite ion concentrations which are almost equal to those of the human blood plasma (*i.e.*, Na^+ 142.0, K^+ 5.0, Mg^{2+} 1.5, Ca^{2+} 2.5, Cl^- 148.8, HCO^{3-} 4.2 and HPO_4^{2-} 1.0 mM). The *in vitro* mineralization ability of a material is often evaluated by examining the ability of apatite to form on its surface in **SBF**, which is useful for predicting the *in vivo* bone bioactivity of a material.[33] The **ACP-PLA** and **HA-PLA** coatings on **Ta** plates

were immersed in **SBF** (20 mL) in culture dishes (diameter, 60 mm), and placed in an incubator at 37 °C. Thereafter, **SBF** (10 mL) in culture dishes was replaced with fresh **SBF** (10 mL) every day. The surface morphologies of the mineralized **ACP-PLA** and **HA-PLA** modified **Ta** plates were withdrawn for characterization on day of 0, 1, 3 and 7, respectively.

2.5 The measurement of sustained BSA release

A protein of bovine serum albumin (**BSA**, Sangon Biotech Ltd., China) has been chosen to prepare the **BSA**-containing **ACP-PLA** and **BSA**-containing **HA-PLA** suspensions for coating **Ta** plates (1 cm × 1 cm × 0.1 mm). The **BSA**-containing **ACP** nanospheres and **HA** nanorods were prepared according to the modified method used in the preparation of growth factors-containing **ACP-PLA** and **HA-PLA** modified **Ta** scaffolds. The 30 mg of **ACP** or **HA** were separately dispersed in **BSA** solution (5 mL, 1 mg mL^{-1}). The suspension was shaken at a constant rate of 130 rpm in a sealed vessel at 37 °C for 2 h, followed by freeze-drying to obtain the **BSA**-loading **ACP** nanospheres and **HA** nanorods. The coating process is similar to above preparation process of **ACP-PLA** and **HA-PLA** modified **Ta** scaffolds.

The *in vitro* release experiments were performed as follows: the **BSA**-loading **Ta** plates were immersed into **SBF** (80 mL) at 37 °C under shaking at a rate of 160 rpm. The **BSA** release medium (2 mL) was withdrawn for the UV-vis analysis at 562 nm using the Bicinchoninic Acid Kit (BCA, Beyotime Institute of Biotechnology, China) at given time intervals. The withdrawn solution was replaced with fresh **SBF** (2 mL, 37 °C). Thereafter, the release curves were obtained and used for the analysis of *in vitro* **BSA** release.

2.6 Cell viability and morphology

The **ACP-PLA** or **HA-PLA** modified porous **Ta** scaffolds (0.5 cm × 0.5 cm × 0.5 cm) were prepared for the study of cell viability. The osteoblast-like cells (MG63) were cultured in Dulbecco's Modified Eagle's Medium (**DMEM**) with 10% Fetal Bovine Serum (**FBS**) and 1% penicillin–streptomycin in an in humidified incubator at 37 °C with 5% CO_2. The different samples were sterilized by 75% ethanol in the 48-well culture plates (Coning, USA). The bare porous **Ta** scaffolds were used as controls. Then, cell suspension (1.0 mL, 1×10^5 cell mL^{-1}) were seeded onto the **ACP-PLA** and **HA-PLA** modified porous **Ta** scaffold, and cultured for 24 hours. Then, these scaffolds were transferred into new 48-well culture plates, and fresh culture medium was added. After being cultured for given time, a microplate reader (MK3, Thermo, USA) was used to determine the accumulated reduction of alamarBlue™ (Gibco company, USA) in the culture medium on the day of 1 and 3, at extinction wavelength of 570 and 600 nm. The accumulation reduction of alamarBlue™, which is directly related to the reduced internal environment of the cells, can be calculated by the light absorption variation of the reagent from the oxidized blue to the reduced red state. It was reported that the viability of MG63 cells cultured on the scaffolds was evaluated through the change of reduction of alamarBlue™.[34] Operation procedures, calculation of cell proliferation and viability were performed according to the instructions of alamarBlue™ assay.

The morphology of MG63 was obtained under SEM. Firstly, the sample was rinsed by phosphate-buffered saline (**PBS**) to remove unattached cells, and then was fixed in 2.5% glutaraldehyde solution for 30 min. The fixed cells were dehydrated by ethanol solutions with increased concentrations (30, 50, 75, 95 and 100 vol%) for 10 min. Finally, the dehydrated samples were air-dried and sputter coated with gold and observed with SEM (S-3400, HITACHI, Japan) at a voltage of 15 kV.

Moreover, the confocal laser scanning microscopy (CLSM) was used to investigate the morphology of the MG63 cells seeded on the **ACP-PLA** and **HA-PLA** coatings. After culture for 48 h, the samples were taken out and rinsed with **PBS** to remove the non-adherent cells. The adherent cells were fixed in 4% paraformaldehyde, and then washed with **PBS** three times. Then the samples were treated with 0.1% Triton X-100 in **PBS** for 2 min, washed with **PBS** three times, and then the nonspecific binding sites were blocked with 1% **BSA** in **PBS** for 20 min. The actin cytoskeletons were labeled in green by incubating with phalloidin-**FITC** (Sigma) for 60 min. After rinsing with **PBS** three times, the cell nuclei were stained in blue by 4′,6-diamidino-2-phenylindole dihydrochloride (**DAPI**, Sigma) for 10 min and washed with **PBS** three times. Finally, the confocal laser scanning microscopy (Leica, SP8, Germany) was used to visualize the actin cytoskeletons and the nuclei of the cells.

2.7 *In vivo* investigation of subchondral bone defect repair

Articular cartilage and subchondral bone defects (5 mm wide, and 1 cm depth) were created on the femoral trochlear groove of left hind femur of mature New Zealand white rabbits (3.0 kg) using electric drill, after a general anaesthetic with pentobarbital sodium solution (3%, 30 mg kg^{-1}). Ethical approval was given by Independent Ethics Committee, Changzheng Hospital, Second Military Medical University (Shanghai, China). The defects areas were filled with the bare porous **Ta** scaffolds, and two kinds modified porous **Ta** scaffolds with **ACP-PLA** or **HA-PLA** coatings with **VEGF**/**TGF** (5 μg **VEGF**121 and 2 μg **TGF-β1** in loading solution, PeproTech Inc., USA). Then, the autogenic periosteums (10 mm wide) separated from marginal area of the same condyles were used to cover the defects. Each kind of scaffolds was sterilized by 75% ethanol, washed with **PBS** and then placed into 3 defect sites for evaluation following surgery. The cast plasters were used to immobilize the joints for 2 weeks, and the samples were harvested at 12 weeks. The collected samples were subsequently fixed in 10% phosphate buffered formalin for 48 h before the dehydration treatment in a series of ethanol (75, 85, 95 and 100 vol%). The femoral samples were then decalcified in 10% **EDTA**, changed twice weekly for 3 weeks, and then embedded in paraffin with the long axis parallel to the base plane. Thereafter, these samples were sliced into thin specimens (5 μm) parallel to the long axis of the condyles. The thin specimens were mounted on poly-L-lysine-coated slides and then subjected to be stained with the Van Gieson, Toluidine blue and Masson's trichrome methods for the analysis of histology.

3. Results and discussion

3.1 Characterization of ACP nanospheres and HA nanorods

The structures of the as-prepared **ACP** and **HA** are investigated with TEM. As shown in Fig. 1a and b, the **ACP** shows a nanospherical structure with diameters of 10–50 nm, and the selected area electron diffraction (SAED) pattern shows an amorphous structure (Fig. 1c). Meanwhile, the XRD pattern (Fig. 2a) which shows no discernable peaks of crystalline **CaP** but a characteristic hump of amorphous phase at around $2\theta = 30^\circ$ also indicates that the sample is consisted of **ACP** phase. The formation mechanism of **ACP** nanosphere has been studied in previous reports.[31] The block copolymer of **PLA-mPEG** which has been widely used in drug release is amphiphilic and can easily self-assemble to form spherical micelle in aqueous solution. The negatively charged oxygen atoms of C–O–C groups in the **PLA-mPEG** chains may interact with Ca^{2+} ions *via* electrostatic attraction.[35] The presence of poly(ethylene glycol) chains is known to decrease the solubility of the amorphous phase and inhibit its transformation to HAP.[36]

Meanwhile, the TEM micrographs in Fig. 1d and e indicate that the **HA** is consisted of nanorod structure with diameters of 20–30 nm. The SAED pattern (Fig. 1f) of an individual nanorod shows a single-crystalline diffraction pattern of **HA**. The XRD pattern of the **HA** nanorods is given in Fig. 2a, and shows that the sample is consisted of a single phase of a hexagonal structure (JCPDS no. 09-0432). The diffraction peaks of **HA** nanorods at around $2\theta \approx 25.8^\circ$, 28.9°, 31.7°, 34.0°, 40.5°, 46.7°, 49.5°, 53.1° and 64.1° correspond to (002), (210), (211), (202), (221), (222), (213), (004) and (304) crystal faces of **HA**. The preferred growth direction of the **HA** nanorod is along the *c*-axis of the hexagonal structure. The formation of **HA** nanorods can be well explained by a crystallization process of **ACP** nanospheres and the following crystal growth, under the hydrothermal treatment at 200 °C for 24 h.

It is difficult to directly coat **ACP** or **HA** onto the surface of **Ta** metals at normal conditions. Therefore, **PLA** which is a popular biomaterial was chosen to make composites with **ACP** or **HA**, and used as adhesion agent to coat **ACP** or **HA** onto the surface of **Ta** metals. The as-prepared **ACP** nanospheres and **HA** nanorods can be well dispersed in acetone (inset of Fig. 2a), and used to prepare homogeneous suspensions after being blended with **PLA** polymer. Then, the **ACP-PLA** and **HA-PLA** suspensions were separately used to modify the **Ta** scaffolds. The main strategy for the preparation of **ACP-PLA** and **HA-PLA** modified **Ta** scaffolds is illustrated in Scheme 1. After the coating procedure, the **ACP-PLA** or **HA-PLA** layers are easily obtained on the surface of **Ta** scaffolds.

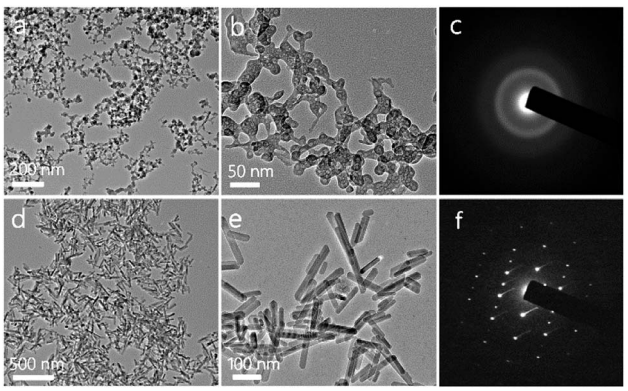

Fig. 1 TEM micrographs and SAED patterns of **ACP** nanospheres and **HA** nanorods. (a and b) TEM micrographs of **ACP** nanospheres; (c) SAED pattern of **ACP** nanospheres; (d and e) TEM micrographs of **HA** nanorods; (f) SAED pattern of **HA** nanorods.

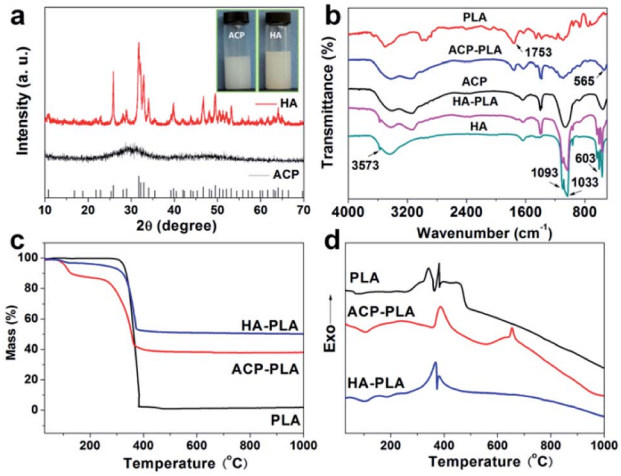

Fig. 2 Characterizations of **ACP** nanospheres, **HA** nanorods, **ACP-PLA** and **HA-PLA**. (a) XRD patterns of **ACP** nanospheres and **HA** nanorods, and the insets show the optical photographs of the dispersed **ACP** nanospheres and **HA** nanorods in acetone; (b) FTIR spectra of pure **PLA** polymer, **ACP** nanospheres, **HA** nanorods, and **ACP-PLA**/**HA-PLA** detached from modified **Ta** plates; (c) TG and (d) DSC curves of **PLA**, **ACP-PLA** and **HA-PLA**.

3.2 Characterization of ACP-PLA and HA-PLA

FTIR spectra of the pure **PLA**, **ACP** nanospheres, **HA** nanorods and the composites of **ACP-PLA** and **HA-PLA** are shown in Fig. 2b. In the spectra of pure **PLA**, **ACP-PLA** and **HA-PLA**, the following absorption peaks are observed, including the C–O stretching at about 1087 cm^{-1}, carbonyl band (–C=O) at about 1753 cm^{-1}, and –CH– stretching vibration at about 3000 cm^{-1}.[37] These characteristic peaks imply the presence of the **PLA** polymer. For the FTIR spectra of **ACP** nanospheres, **HA** nanorods, **ACP-PLA** and **HA-PLA**, the distinctive bands at around 565, 603, 1033 and 1093 cm^{-1} for PO_4^{3-} are observed, indicating the presence of **ACP** and **HA**.[12,21] The results of FTIR spectra support

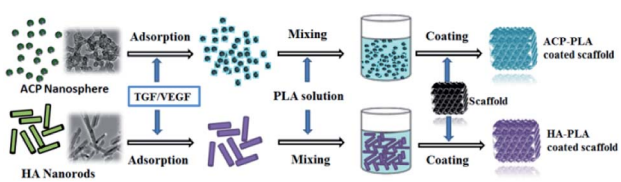

Scheme 1 Illustration of the strategy for the preparation of **ACP-PLA** and **HA-PLA** modified **Ta** scaffolds.

the existence of **ACP**, **HA** and **PLA** in the composites of **ACP-PLA** and **HA-PLA**, respectively.

The TG and DSC curves are obtained to investigate the thermophysical properties of the **PLA** polymer and **ACP-PLA** and **HA-PLA** (Fig. 2c and d). In the TG curve of **PLA**, about 100% weight loss is observed in the temperature range of 300–400 °C, due to the oxidative decomposition of **PLA** polymer, accompanying by exothermic peaks near 390 °C in the curve of DSC. In the TG curves of **ACP-PLA** and **HA-PLA**, the weight losses of about 51.9% and 45.3% are due to the oxidative decomposition of the **PLA** in the temperature range of 200–400 °C, which also can be accompanied by the exothermic peaks near 350 °C in the DSC curves. The mass percentages of **PLA** in **ACP-PLA** and **HA-PLA** are about 51.9% and 45.3%, and the mass percentages of **ACP** and **HA** are 38.5% and 51.2%, respectively. The difference between this results and the input qualities of **ACP** and **HA** may be attributed to the difference on the water contents in the samples. The weight losses of about 9.6% and 3.5% in the temperature range of 100–120 °C in the TG curves is due to the loss of water molecules in **ACP-PLA** and **HA-PLA**, which can be accompanied by endothermic peaks near 100 °C in the DSC curves, respectively. Otherwise, there is a small peak in the DSC curves of **ACP-PLA** around 650 °C corresponding to the phase transform of amorphous to crystalline **CaP** at high temperatures. This result accords with the result of XRD pattern which has indicated an amorphous phase of **ACP** nanospheres. The above results of both TG and DSC curves display the thermophysical properties of the as-prepared **PLA**, **ACP-PLA** and **HA-PLA**, supporting the existence of **ACP**, **HA**, and **PLA** in the composites of **ACP-PLA** and **HA-PLA**, respectively.

3.3 *In vitro* mineralization of ACP-PLA and HA-PLA modified Ta plates

The bare **Ta** plates, **PLA** modified **Ta** plates were treated in **SBF** for different days and observed by SEM (Fig. 3). There is no new substance precipitated on the surfaces of bare **Ta** plates and **PLA** coating on **Ta** plates after being immersed in **SBF** for 7 days. However, the surface morphologies of **ACP-PLA** and **HA-PLA** coatings on **Ta** surfaces largely change after being immersed in **SBF** for different time (Fig. 3). Before the treatment with **SBF**, the **ACP** nanospheres and **HA** nanorods are embedded in **PLA** polymer and form **ACP-PLA** and **HA-PLA** coatings on the surfaces of **Ta** plates. However, the surface of the **ACP-PLA** coating on **Ta** plates are covered by assembled structures of **CaP** nanosheets after being immersed in **SBF** for only 1 day. With expanding the time from 1 day to 3 days and 7 days, the size of **CaP** nanosheets gradually grows up. It is well reported that the **ACP** is not stable and can transform into crystallized **HA** in aqueous solution.[38,39] As for the **HA-PLA** coating on **Ta** plates, there is no obvious shape transformation but a size change of **HA** nanorods after being immersed in **SBF** for 1 day. Thereafter, a lot of new **HA** nanorods appear on the surfaces of **HA-PLA** modified **Ta** plates, after expanding the time from 1 day to 3 days and 7 days. The early mineralization property of biomaterials in one week is important for studying the bioactivity of biomaterials.[40,41] After the early mineralization process, the further mineralization might induced by the resultant minerals on the surface of biomaterials but not the real surface of biomaterials. Therefore, it has been generally considered to have a good bioactivity for the biomaterials that can quickly promote the formation of hydroxyapatite on their surface in **SBF**.[42]

Furthermore, the mass changes of the **ACP-PLA** and **HA-PLA** modified **Ta** plates are measured in the process of mineralization (Fig. 4). The masses of both **ACP-PLA** and **HA-PLA** modified **Ta** plates do not show obvious change in first day. Then, the mass of the **ACP-PLA** and **HA-PLA** modified **Ta** plates increase ~0.20 and ~0.17 mg cm^{-2} after 3 days of mineralization. After expanding mineralization time to 7 days, the masses of the **ACP-PLA** and **HA-PLA** modified **Ta** plates continually increase ~0.65 and ~0.60 mg cm^{-2}. After mineralization in **SBF**, the **CaP** nanosheets are found everywhere on the surface of **ACP-PLA** modified **Ta** plates. The transform from **ACP-PLA** composite to crystalline nanosheets can be explained by the crystal transformation and following crystal growth. The **ACP** content in the **ACP-PLA** can crystallize to reach a thermodynamically and

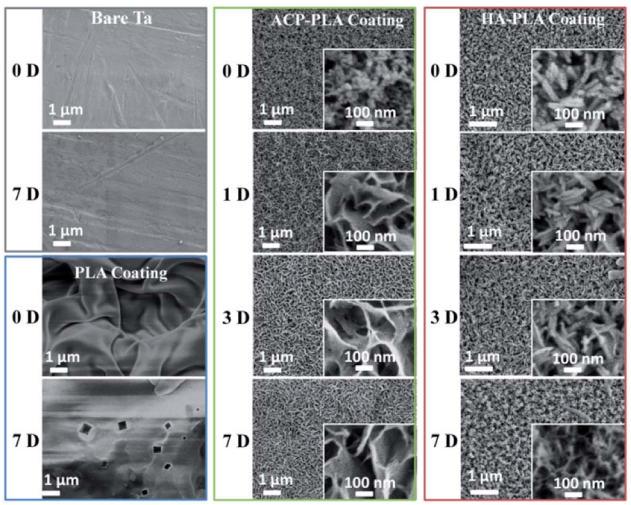

Fig. 3 SEM micrographs of bare Ta plates, and PLA, ACP-PLA and HA-PLA modified Ta plates treated in SBF for different time.

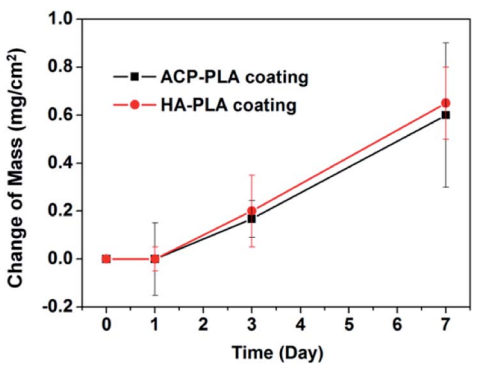

Fig. 4 The mass changes of ACP-PLA and HA-PLA modified Ta plates *versus* the time of mineralization in SBF. Data are presented as mean ± standard deviation (SD), and number of replicates (*n*) is three.

chemically stable phase of **HA**, when the sample is immersed into **SBF** at 37 °C with a pH value of 7.4. In the early stage, the crystal phase of inorganic component in **ACP-PLA** is transformation from **ACP** to **HA**. Thereafter, the ions of calcium and phosphate in **SBF** can form new precipitate of **HA** and promote the growth of the primarily formed **HA** structures. The increase in mass after the mineralization for 3 and 7 days can prove the above results. As for the **HA-PLA**, there is no phase transformation when the samples were immersed in **SBF**. However, the abound ions of calcium and phosphate in the solution can form new precipitate of **HA** and promotes the growth of the primary **HA** nanorods. Therefore, the different surface morphologies of **ACP-PLA** and **HA-PLA** modified **Ta** plates are observed after being immersed in **SBF**.

The hypothetical mechanisms of the mineralization on the surface of **ACP-PLA** and **HA-PLA** modified **Ta** plates in **SBF** are exhibited in Fig. 5. The **ACP** nanospheres and **HA** nanorods which are individually blended in the **PLA** play key roles of seeds for the formation of **HA**. The different final surface structures after mineralization can be explained by the different dominant growth of the **HA** crystal on the surface of **ACP-PLA** and **HA-PLA** modified **Ta** plates. The **ACP** nanospheres with an amorphous phase do not guide the direction of crystallization and crystal growth at the initial stage. Therefore, the products of spherulites composed of platelet crystallites organized in radial orientation are obtained, due to the disordered crystallization of **ACP** nanospheres.[43] Then, the products with nanosheets structure can formed by the way of crystal growth using the abundant Ca^{2+} and PO_4^{3-} ions in the **SBF**. On the other hand, the **HA** nanorods do not have the crystallization process. The main change of **HA-PLA** modified **Ta** plates in mineralization is the crystal growth and new formation of **HA**. There is a specific preferred growth direction which is along the *c*-axis of the hexagonal **HA**. Therefore **HA** nanorods may induce the growth direction of the new formed **HA** products on the surface of **HA-PLA** modified **Ta** plates.

Contact angles on the different surfaces of the as-prepared **ACP-PLA** and **HA-PLA** coatings on **Ta** plates with or without treatment of mineralization in **SBF** are measured using deionized water. Sharp decreased contact angles of water on **ACP-PLA** and **HA-PLA** are observed which occurred after 1 and 7 days of mineralization in **SBF** (Fig. 6). After the mineralization, the surface of both samples became absolutely hydrophilic, which can be well explained by the formation of porous structures of **HA** nanosheets and **HA** nanorods. The spreading of the droplet may be driven by capillary effects within porous structures of **HA** nanosheets and **HA** nanorods formed on the surface of **ACP-PLA** and **HA-PLA** after the mineralization in **SBF**.

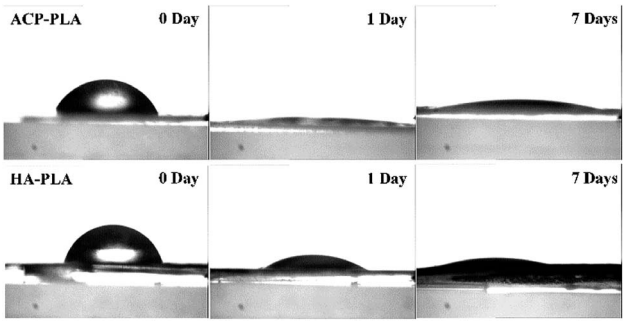

Fig. 6 Contact angles on the surfaces of ACP-PLA and HA-PLA modified Ta plates before and after mineralization for 1 and 7 days in SBF.

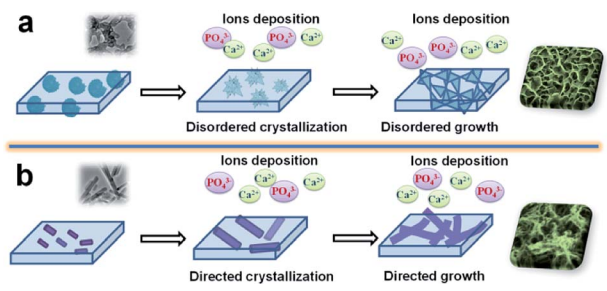

Fig. 5 The hypothetical mechanism for the mineralization of ACP-PLA and HA-PLA modified Ta scaffolds in SBF. (a) ACP-PLA modified Ta scaffolds; (b) HA-PLA modified Ta scaffolds.

3.4 *In vitro* growth factor/BSA loading and release

The adsorption efficiency of growth factor by **ACP** nanospheres and **HA** nanorods were studied by measure the amount of **VEGF-FITC** in supernatants (Fig. S1†). After centrifugal separation of **VEGF-FITC**-loading **ACP** nanospheres and **HA** nanorods from the solution, the supernatants were obtained and measured with a fluorescence spectrometer. The amounts of **VEGF-FITC** in supernatants were calculated as 1.44 μg and 1.36 μg for the loading solution of **ACP** nanospheres and **HA** nanorods, respectively. The results indicate that 5.56 μg and 5.64 μg of **VEGF-FITC** were adsorbed by **ACP** nanospheres and **HA** nanorods, and adsorption efficiency are 79.4% and 80.6%, respectively. The fluorescence micrographs of **ACP** nanospheres and **HA** nanorods after loading with **VEGF-FITC** were also obtained, which indicate a good adsorption effect of both samples (Fig. 7).

Then, we also studied the drug release properties of **ACP-PLA** and **HA-PLA** coating. Firstly, the methods of fluorescence spectrum and ELISA kit have been used to investigate the release amount of **VEGF** at different time from these coatings. Unfortunately, it is too difficult to exactly measure the release amount of these growth factors in the medium of **SBF** which were released from the coatings. The amount of growth factors in **ACP-PLA** or **HA-PLA** on the surface of **Ta** scaffolds is very small, and the released amount of these molecules in **SBF** is smaller. Therefore, the typical protein molecule of **BSA** has been selected, which has been widely used as a drug model in the biomedical research. The sustained drug release behaviors of **BSA**-containing **ACP-PLA** and **HA-PLA** coatings on **Ta** plates are investigated in **SBF** at 37 °C. As the curve in Fig. 8a shown, the release rate of **BSA** from **ACP-PLA** modified **Ta** plates is rapid in the first 3 days, and then reduces gradually. The cumulative release account from **ACP-PLA** modified **Ta** plates reaches to 15.6, 17.6, 18.8 and 21.8 μg cm^{-2} at the time of 5, 10, 19 and 29

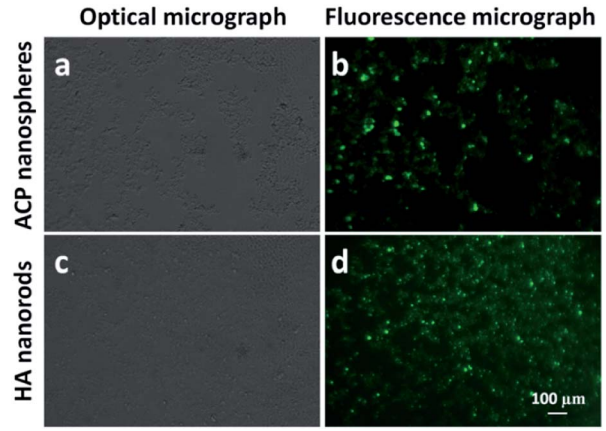

Fig. 7 Optical and fluorescence micrographs of ACP nanospheres and HA nanorods loaded with VEGF-FITC. (a) Optical micrograph and (b) fluorescence micrograph of ACP nanospheres loaded with VEGF-FITC; (c) optical micrograph and (d) fluorescence micrograph of HA nanorods loaded with VEGF-FITC.

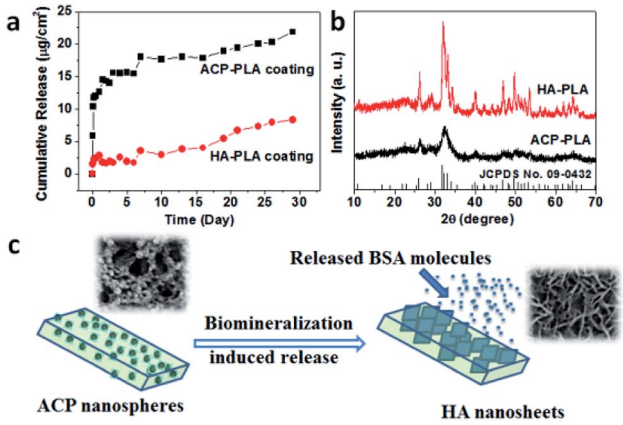

Fig. 8 (a) Cumulative BSA release curves from ACP-PLA and HA-PLA modified Ta plates; (b) the XRD patterns of the ACP-PLA and HA-PLA after the *in vitro* BSA release; (c) the hypothetical mechanism for the *in vitro* BSA release from the ACP-PLA modified Ta plates.

days. Meanwhile, the release rate from **HA-PLA** modified **Ta** plates is slower than **ACP-PLA**. The cumulative **BSA** release from **HA-PLA** modified **Ta** plates reaches to 2.0, 2.9, 5.4 and 8.4 μg cm^{-2} at the time of 5, 10, 19 and 29 days.

The above different release curves can be explained by the different structure and mineralization process on the surfaces of **ACP-PLA** and **HA-PLA** modified **Ta** plates. The initial rapid **BSA** release from the **ACP-PLA** modified **Ta** plates can be explained by the changes of structure and morphology. In the early **BSA** release process, the crystal phase transformation from **ACP** to crystalline **HA** occurred in **SBF**. In this way, the structural remodeling on the surface of the **ACP-PLA** modified **Ta** plates can lead a rapid release of **BSA** which is loaded by the **ACP** nanospheres through the adsorption. The result of XRD pattern in Fig. 8b indicates that the crystal phase of **ACP-PLA** has transformed from **ACP** to **HA** (JCPDS no. 09-0432) after the release process in **SBF** for 29 days. The hypothetical release mechanism of **ACP-PLA** is illustrated in Fig. 8c. On the other hand, as shown in the result of XRD (Fig. 8b), there is no obvious crystal phase change of the as-prepared **HA-PLA** modified **Ta** plates after the **BSA** release in **SBF**. The stable crystal phase may contribute to the slower **BSA** release. Meanwhile, the structures and morphologies of **ACP** nanospheres and **HA** nanorods are different, which may result in different surface properties and specific surface area, and may further influence on their drug release properties. It well reported that the size and specific surface area of drug carriers displays important influence on drug release properties.[44,45]

3.5 Cell viability

The cytotoxicity of bare **Ta** and **ACP-PLA** and **HA-PLA** modified **Ta** scaffolds are investigated using MG63 cells (Fig. 9). The alamarBlue™ assay reveals that there is essentially no toxicity when the cells are cultured on bare **Ta**, **ACP-PLA** and **HA-PLA** modified porous **Ta** scaffolds. On the first day, the difference of the cell viabilities among these samples is not obvious. With increasing culturing time from 1 day to 3 days and 7 days, the viabilities of MG63 cells are higher. The experimental results indicate that MG63 cells grow well on **ACP-PLA** and **HA-PLA** modified porous **Ta** scaffolds.

The SEM micrographs of MG63 cells seeded on the bare **Ta** scaffolds, **ACP-PLA** and **HA-PLA** modified porous **Ta** scaffolds after culture for 3 days are shown in Fig. 10. The magnified SEM micrographs in Fig. 10a–d indicate a good state of MG63 cells. The cells are better attaching and spreading on the surface of the **ACP-PLA** and **HA-PLA** modified porous **Ta** scaffolds than the bare **Ta** scaffolds. The antenna-like parts of the MG63 cells are observed on the surface of **ACP-PLA** and **HA-PLA** modified porous **Ta** scaffolds, indicating a good interconnection between the cells and **ACP-PLA** and **HA-PLA** modified porous **Ta** scaffolds.

Moreover, the spreading behavior of MG63 cells cultured on the as-prepared **ACP-PLA** and **HA-PLA** modified **Ta** scaffolds are investigated by CLSM (Fig. 11), after culturing for 48 h. The bare **Ta** plates are used as the control samples. The actin

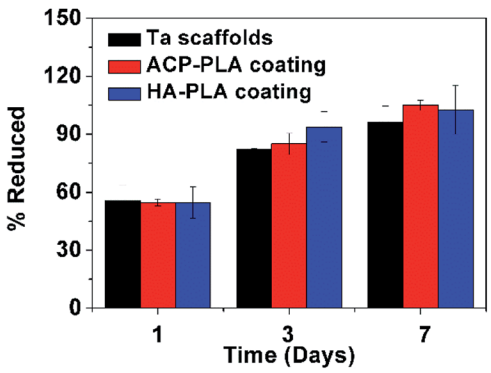

Fig. 9 Percentage of alamarBlue™ reduction for MG63 cells on the bare Ta, ACP-PLA and HA-PLA modified porous Ta scaffolds. Data are presented as mean ± standard deviation (SD), and number of replicates (*n*) is three.

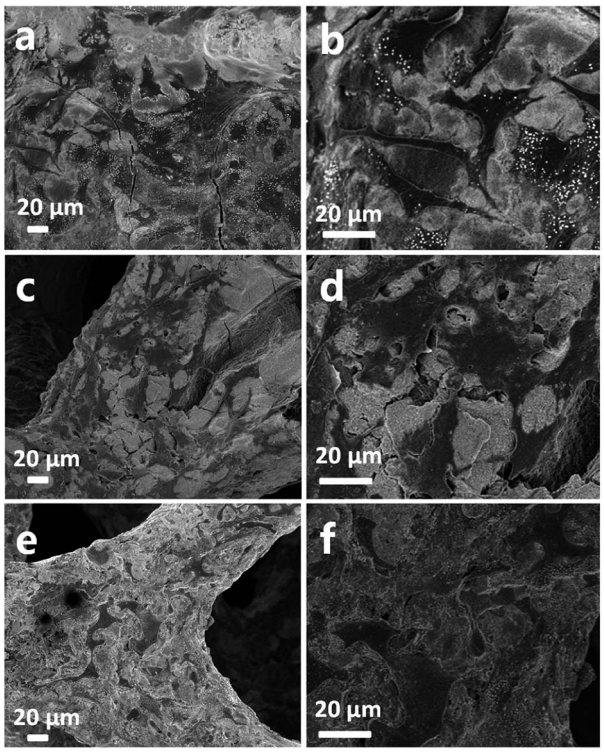

Fig. 10 SEM micrographs of MG63 cells cultured on the ACP-PLA, HA-PLA modified porous Ta scaffolds and bare porous Ta scaffolds for 3 days. (a and b) ACP-PLA modified porous Ta scaffolds; (c and d) HA-PLA modified porous Ta scaffolds; (e and f) bare porous Ta scaffolds.

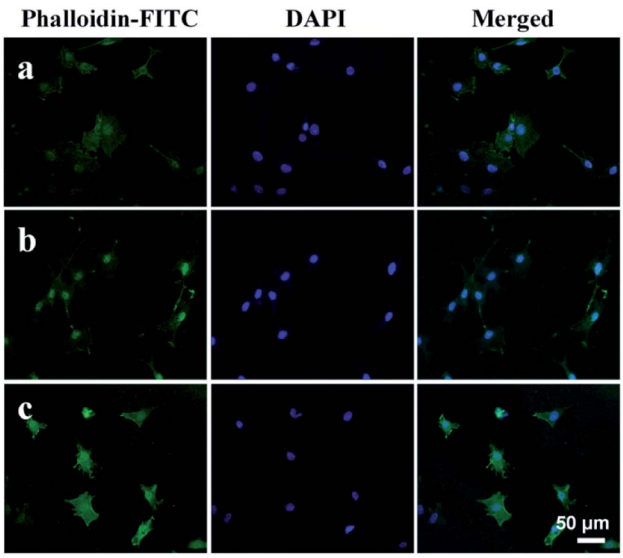

Fig. 11 Confocal laser scanning microscopy micrographs of MG63 cells on different scaffolds, after culturing for 48 h. (a) ACP-PLA modified Ta scaffolds; (b) HA-PLA modified Ta scaffolds; (c) bare Ta scaffolds.

cytoskeletons are labeled in green by phalloidin-**FITC**, and the cell nuclei are stained in blue by **DAPI**. As shown in the Fig. 11, many cells with filopodia on the **ACP-PLA** and **HA-PLA** modified **Ta** plates can be observed. The result indicates that the **ACP-PLA** and **HA-PLA** modified **Ta** exhibits excellent properties on cell spreading, because of the MG63 cells appear cytoplasmic extensions and filopodia attachments, which is the typical morphology of osteoblast. For the control sample of bare **Ta** scaffolds (Fig. 11c), MG63 cells also appear good typical morphology of osteoblast, after being seeded for 48 h. These results indicate that bare **Ta** scaffolds, the as-prepared **ACP-PLA** and **HA-PLA** modified **Ta** scaffolds have good properties on cell spreading.

3.6 *In vivo* investigation of subchondral bone defect repair

The preliminary *in vivo* experiments have been carried out to evaluate the bone defect repair performance of the samples. All experimental animals are healthy with free movable joints, after implanting the two kinds of modified **Ta** scaffolds and bare **Ta** scaffolds for 12 weeks. Comparing to healthy femoral trochlear groove (Fig. 12a1), the defective femoral trochlear grooves in

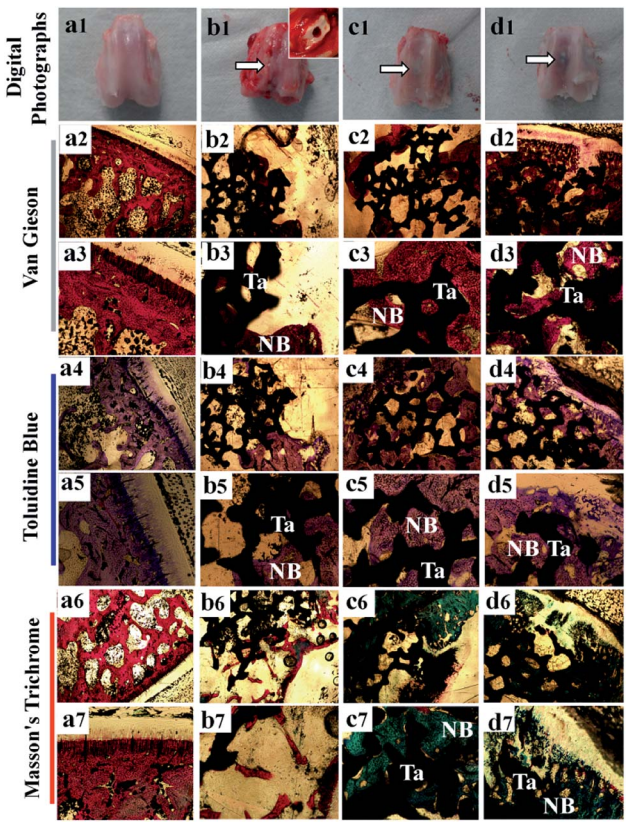

Fig. 12 Digital photographs and photomicrographs of normal bone tissue slices and defective bone tissue slices filled with different scaffold. Digital photographs (a1–d1) and photomicrographs of normal bone tissue slices (a), defective bone tissue slices after being filled with bare Ta (b), ACP-PLA modified porous Ta scaffold (c), and HA-PLA modified porous Ta scaffold (d), after Van Gieson (a2–d2 and a3–d3), Toluidine blue (a4–d4 and a5–d5) and Masson's trichrome staining (a6–d6 and a7–d7). The locations of Ta scaffolds (Ta) and new bone tissue (NB) are marked in amplified micrographs. The magnification of the micrographs are ×40 (a2–d2, a4–d4 and a6–d6) and ×100 (a3–d3, a5–d5 and a7–d7).

experimental groups are well repaired with smooth surfaces after being grafted with bare **Ta** and two kinds of modified porous **Ta** scaffolds (Fig. 12b1–d1), indicating that the bare **Ta**, and two kinds of modified **Ta** scaffolds can promote the bone defect repair.

The photomicrographs of bone slices with Van Gieson, Toluidine blue and Masson's trichrome staining, as well as the control groups of healthy bone tissue are exhibited in Fig. 12. As the results in Fig. 12c3 and d3 shown, new collagen constituent can be observed in two kinds of modified porous **Ta** scaffolds. The bone cells can migrate and grow well in the porous **Ta** scaffolds. The photomicrographs of Toluidine blue (Fig. 12c4, d4, c5 and d5) and Masson's trichrome (Fig. 12c6, d6, c7 and d7) staining also show much deposition of extracellular bone-like matrix on the surface and internal space of **ACP-PLA** modified porous **Ta** scaffolds and **HA-PLA** modified porous **Ta** scaffolds. The cell nuclei have been stained as black dots in the photomicrographs, and the collagen constituents have been stained with bluish green color. Comparing with the bare **Ta** scaffold (Fig. 12b2–b7), the amount of cells and collagen constituent on the **ACP-PLA** and **HA-PLA** modified porous **Ta** scaffolds are more obvious, which indicate good properties for bone defect repair. Meanwhile, the new bone tissue and bone linking in the defect area of the control group is scanty after surgical operation for 12 weeks. These results indicate that the amounts of the new bone tissue and many callus bridges are similar in both modified porous **Ta** scaffold, which are better than that in bare porous **Ta** scaffold.

4. Conclusions

The **ACP** nanospheres and **HA** nanorods are prepared and used with **PLA** polymer to modify **Ta** scaffolds. The effects of **ACP** nanospheres and **HA** nanorods on the mineralization, drug release, cytotoxicity and *in vivo* bone defect repair have been investigated. In the process of mineralization, the structures of **HA** nanosheets and **HA** nanorods are respectively observed on the surfaces of **ACP-PLA** and **HA-PLA** modified **Ta** plates. The **ACP** and **HA** play a key role of seed to guide the crystal growth of minerals. Meanwhile, after the mineralization, the surface of **ACP-PLA** and **HA-PLA** coating become absolutely hydrophilic. The *in vitro* **BSA** release rate of **ACP-PLA** modified **Ta** scaffolds is much faster than **HA-PLA** modified **Ta** scaffolds, which can be explained by the crystal phase transformation from **ACP** to **HA** and the crystallization process. The MG63 cells show good viability and adhesion/spreading behavior on the **ACP-PLA** and **HA-PLA** modified porous **Ta** scaffolds. In the *in vivo* experiment, much of new bone tissues have been observed in the **ACP-PLA** and **HA-PLA** modified porous **Ta** scaffolds, indicating a good potential application of these materials in bone defect repair.

Conflicts of interest

There are no conflicts to declare.

Acknowledgements

The financial support from the National Natural Science Foundation of China (31771081, 81171727), the Science and Technology Commission of Shanghai Municipality (18ZR1445100, 19441901900, 19ZR1439700), and S&T Innovation 2025 Major Special Programme of Ningbo (2018B10040) is gratefully acknowledged.

Notes and references

1 T. Garg and A. K. Goyal, *Expert Opin. Drug Delivery*, 2014, **11**, 767–789.
2 J. M. Holzwarth and P. X. Ma, *Biomaterials*, 2011, **32**, 9622–9629.
3 M. A. Fernandez-Yague, S. A. Abbah, L. McNamara, D. I. Zeugolis, A. Pandit and M. J. Biggs, *Adv. Drug Delivery Rev.*, 2015, **84**, 1–29.
4 A. El-Ghannam, *Expert Rev. Med. Devices*, 2005, **2**, 87–101.
5 V. Kesireddy and F. K. Kasper, *J. Mater. Chem. B*, 2016, **4**, 6773–6786.
6 N. Ramesh, S. C. Moratti and G. J. Dias, *J. Biomed. Mater. Res., Part B*, 2018, **106**, 2046–2057.
7 J. D. Bobyn, G. J. Stackpool, S. A. Hacking, M. Tanzer and J. J. Krygier, *J. Bone Jt. Surg., Br. Vol.*, 1999, **81B**, 907–914.
8 R. M. Meneghini, D. G. Lewallen and A. D. Hanssen, *J. Bone Jt. Surg., Am. Vol.*, 2008, **90**, 78–84.
9 Y. Minoda, A. Kobayashi, M. Ikebuchi, H. Iwaki, F. Inori and H. Nakamura, *J. Arthroplasty*, 2013, **28**, 1760–1764.
10 K. Rezwan, Q. Z. Chen, J. J. Blaker and A. R. Boccaccini, *Biomaterials*, 2006, **27**, 3413–3431.
11 E. Verron, J. M. Bouler and J. Guicheux, *Acta Biomater.*, 2012, **8**, 3541–3551.
12 S. V. Dorozhkin, *Acta Biomater.*, 2010, **6**, 4457–4475.
13 A. K. Bembey, A. J. Bushby, A. Boyde, V. L. Ferguson and M. L. Oyen, *J. Mater. Res.*, 2006, **21**, 1962–1968.
14 M. Tzaphlidou, *J. Biol. Phys.*, 2008, **34**, 39–49.
15 S. Weiner and H. D. Wagner, *Annu. Rev. Mater. Sci.*, 1998, **28**, 271–298.
16 M. A. Rubin, L. Jasiuk, J. Taylor, J. Rubin, T. Ganey and R. P. Apkarian, *Bone*, 2003, **33**, 270–282.
17 V. Uskokovic and D. P. Uskokovic, *J. Biomed. Mater. Res., Part B*, 2011, **96B**, 152–191.
18 M. Motskin, D. M. Wright, K. Muller, *et al.*, *Biomaterials*, 2009, **30**, 3307–3317.
19 C. Qi, Y. J. Zhu, X. Y. Zhao, *et al.*, *Chem.–Eur. J.*, 2013, **19**, 981–987.
20 Q. W. Fu, Y. P. Zi, W. Xu, *et al.*, *Int. J. Nanomed.*, 2016, **11**, 5087–5097.
21 Z. F. Zhou, T. W. Sun, F. Chen, *et al.*, *Biomaterials*, 2017, **121**, 1–14.
22 F. Chen, C. Li, Y. J. Zhu, X. Y. Zhao, B. Q. Lu and J. Wu, *Biomater. Sci.*, 2013, **1**, 1074–1081.
23 F. Chen, P. Huang, Y. J. Zhu, J. Wu, C. L. Zhang and D. X. Cui, *Biomaterials*, 2011, **32**, 9031–9039.
24 E. I. Altinoglu, T. J. Russin, J. M. Kaiser, *et al.*, *ACS Nano*, 2008, **2**, 2075–2084.
25 R. Ravichandran, J. R. Venugopal, S. Sundarrajan, S. Mukherjee and S. Ramakrishna, *Biomaterials*, 2012, **33**, 846–855.

26 H. L. Oliveira, W. L. O. Da Rosa, C. E. Cuevas-Suarez, *et al.*, *Calcif. Tissue Int.*, 2017, **101**, 341–354.
27 H. B. Wen, R. A. J. Dalmeijer, F. Z. Cui, C. A. Van Blitterswijk and K. De Groot, *J. Mater. Sci. Lett.*, 1998, **17**, 925–930.
28 R. Zhou, W. Xu, F. Chen, *et al.*, *Colloids Surf., B*, 2014, **123**, 236–245.
29 K. Mediaswanti, C. Wen, E. P. Ivanova, *et al.*, *Int. J. Surf. Sci. Eng.*, 2014, **8**, 255–263.
30 D. Naskar, A. K. Ghosh, M. Mandal, P. Das, S. K. Nandi and S. C. Kundu, *Biomaterials*, 2017, **136**, 67–85.
31 F. Chen, P. Huang, Y. J. Zhu, J. Wu and D. X. Cui, *Biomaterials*, 2012, **33**, 6447–6455.
32 T. Kokubo, H. Kushitani, S. Sakka, T. Kitsugi and T. Yamamuro, *J. Biomed. Mater. Res.*, 1990, **24**, 721–734.
33 T. Kokubo and H. Takadama, *Biomaterials*, 2006, **27**, 2907–2915.
34 G. Wang, X. Liu, J. Gao and C. Ding, *Acta Biomater.*, 2009, **5**, 2270–2278.
35 S. G. Deng, J. M. Cao, J. Feng, *et al.*, *J. Phys. Chem. B*, 2005, **109**, 11473–11477.
36 Y. Fan, Z. Sun and J. Moradian-Oldak, *Biomaterials*, 2009, **30**, 478–483.
37 M. P. Prabhakaran, J. Venugopal and S. Ramakrishna, *Acta Biomater.*, 2009, **5**, 2884–2893.
38 J. H. Tao, H. H. Pan, J. R. Wang, *et al.*, *J. Phys. Chem. C*, 2008, **112**, 14929–14933.
39 H. Zhang, Q. W. Fu, T. W. Sun, *et al.*, *Colloids Surf., B*, 2015, **136**, 27–36.
40 N. Rauner, M. Meuris, M. Zoric and J. C. Tiller, *Nature*, 2017, **543**, 407–410.
41 N. Cozza, F. Monte, W. Bonani, P. Aswath, A. Motta and C. Migliaresi, *J. Tissue Eng. Regener. Med.*, 2018, **12**, 1131–1142.
42 C. T. Wu, J. Chang and Y. Xiao, *Advanced bioactive inorganic materials for bone regeneration and drug delivery*, CRC Press and Taylor & Francis, 2013.
43 H. Pan, X. Y. Liu, R. Tang and H. Y. Xu, *Chem. Commun.*, 2010, **46**, 7415–7417.
44 S. A. A. Rizvi and A. M. Saleh, *Saudi Pharm. J.*, 2018, **26**, 64–70.
45 G. J. Dawes, L. E. Fratila-Apachitei, K. Mulia, *et al.*, *J. Mater. Sci.: Mater. Med.*, 2009, **20**, 1089–1094.